RAA 2014 Vol. **14** No. **12**, 1578–1594 doi: 10.1088/1674–4527/14/12/007
http://www.raa-journal.org *http://www.iop.org/journals/raa*

***R**esearch in*
***A**stronomy and*
***A**strophysics*

Data processing and preliminary results of the Chang'e-3 VIS/NIR Imaging Spectrometer in-situ analysis *

Bin Liu[1], Chun-Lai Li[1], Guang-Liang Zhang[1], Rui Xu[2], Jian-Jun Liu[1], Xin Ren[1], Xu Tan[1], Xiao-Xia Zhang[1], Wei Zuo[1] and Wei-Bin Wen[1]

[1] Key Laboratory of Lunar and Deep Space Exploration, National Astronomical Observatories, Chinese Academy of Sciences, Beijing 100012, China; *licl@nao.cas.cn*

[2] Key Laboratory of Space Active Opto-Electronics Technology, Shanghai Institute of Technical Physics, Chinese Academy of Sciences, Shanghai 200083, China

Received 2014 July 23; accepted 2014 September 6

Abstract The Chang'e-3 Visible and Near-infrared Imaging Spectrometer (VNIS) is one of the four payloads on the Yutu rover. After traversing the landing site during the first two lunar days, four different areas are detected, and Level 2A and 2B radiance data have been released to the scientific community. The released data have been processed by dark current subtraction, correction for the effect of temperature, radiometric calibration and geometric calibration. We emphasize approaches for reflectance analysis and mineral identification for in-situ analysis with VNIS. Then the preliminary spectral and mineralogical results from the landing site are derived. After comparing spectral data from VNIS with data collected by the M^3 instrument and samples of mare that were returned from the Apollo program, all the reflectance data have been found to have similar absorption features near 1000 nm except lunar sample 71061. In addition, there is also a weak absorption feature between 1750$\sim$2400 nm on VNIS, but the slopes of VNIS and M^3 reflectance at longer wavelengths are lower than data taken from samples of lunar mare. Spectral parameters such as Band Centers and Integrated Band Depth Ratios are used to analyze mineralogical features. The results show that detection points E and N205 are mixtures of high-Ca pyroxene and olivine, and the composition of olivineat point N205 is higher than that at point E, but the compositions of detection points S3 and N203 are mainly olivine-rich. Since there are no obvious absorption features near 1250 nm, plagioclase is not directly identified at the landing site.

Key words: Chang'e-3 — VNIS — in-situ analysis — data processing

1 INTRODUCTION

The mineralogical study of lunar mare basalts helps in understanding the geologic evolution of the Moon (Tompkins & Pieters 1999; Jolliff et al. 2000; Pieters et al. 1993; Williams et al. 1995; Cahill et al. 2009; Elkins Tanton et al. 2002). On 2013 December 14 the Chang'e-3 (CE-3) lunar probe landed at a north latitude of 44.1° and west longitude of 19.5°, a site located in Mare Imbrium. The

* Supported by the National Natural Science Foundation of China.

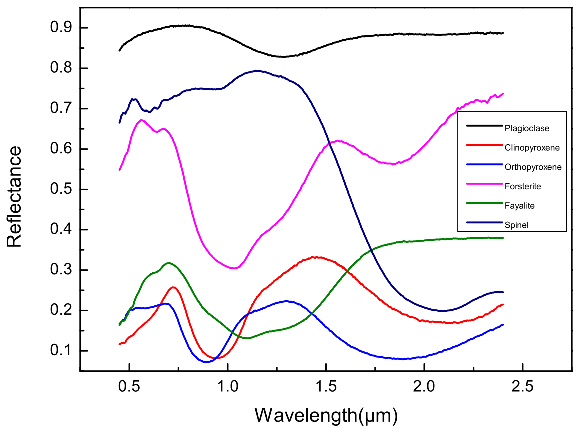

Fig. 1 Main mineral features on the lunar surface.

CE-3 lunar probe contains a lander and a rover. The Visible and Near-infrared Imaging Spectrometer (VNIS) is fixed at the front of the rover and designed to detect lunar minerals through in-situ analysis (Ouyang 2005; Fu et al. 2014; Ip et al. 2014). VNIS contains two channels, which are the Visible and Near-infrared (VNIR) channel and Short Wave Infrared (SWIR) channel. The spectral range of the two channels covers the range from 450 nm to 2400 nm. The main minerals on the lunar surface can be effectively identified in this spectral range, such as pyroxene, olivine and plagioclase (Fig. 1). According to the results of Zhao et al. (2014), the CE-3 landing site is relatively flat and there are two basaltic units around the landing site, low-Ti/very-low-Ti mare basalts in the northern part of Mare Imbrium, and Eratosthenian low-Ti/high-Ti mare basalts in the southern part (Schaber 1969; Hiesinger et al. 2000; Bugiolacchi & Guest 2008; Qiao et al. 2013).

This is the first time that VNIS has been developed for in-situ analysis on the lunar surface. There are two main differences between VNIS in-situ analysis and spaceborne detection. First, the CE-3 exploration mission has the goal of regional detection instead of global observation. It does not include the Cayley Plains area, which is used as a reflectance calibration standard (Pieters 1999; Pieters et al. 2009; Ohtake et al. 2010; Yamamoto et al. 2011). The second difference is the viewing geometry; spaceborne spectrometers mostly view the lunar surface at the nadir point and work at a high solar elevation angles; due to changes in the rover's temperature, VNIS must work at a lower solar elevation angle and tilt 45° to look at the lunar surface. Based on the above differences, the methods used for VNIS data processing are different from spaceborne spectrometers, especially the methods for reflectance analysis and photometric calibration.

After the first exploration mission that lasted two lunar days, VNIS detected four different areas and the radiance data were released. In this study, we will first describe the principle of VNIS and its data products. We also present the reflectance analysis and mineral identification methods for VNIS. The results will demonstrate the spectral and mineralogical features of the landing site.

Section 2 gives the description of VNIS configuration and working principle. Section 3 describes the VNIS data acquired and preprocessing methods. Section 4 introduces the methods for reflectance conversion and mineral identification. Section 5 gives the preliminary results on reflectance analysis and mineralogical analysis. Section 6 describes the main conclusion of the article.

2 DESCRIPTION OF VNIS

VNIS was designed by the Shanghai Institute of Technical Physics, Chinese Academy of Sciences, and was carried on the lunar rover platform (Fig. 2). The entire system was composed of the probe

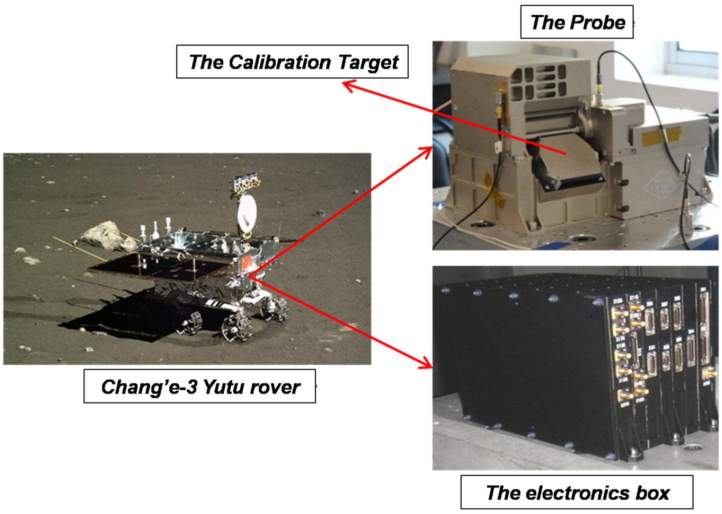

Fig. 2 Construction of VNIS and its position on the rover.

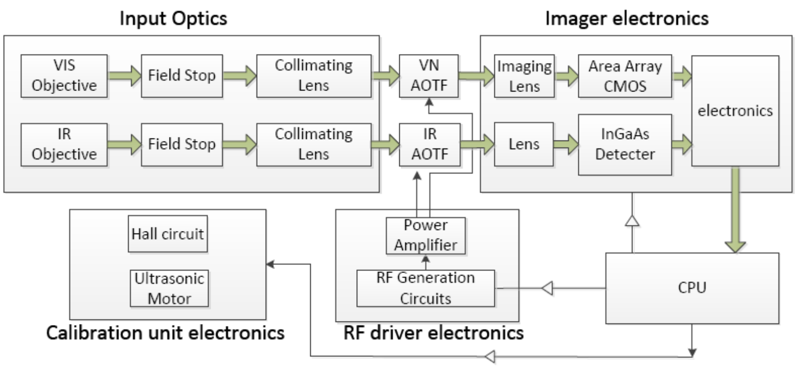

Fig. 3 The configuration of the VNIS system.

and the electronics box (Fig. 2) (He et al. 2011, 2014). The probe was installed at the front of the rover and was inclined 45° with respect to the lunar surface, and the electronics box was installed inside the rover's cabin.

As shown in Figure 3, the solar irradiance reflected by the lunar surface is detected by the VNIS imaging lens, which uses a collimating mirror to make a parallel beam and which is then directed towards an Acousto-Optic Tunable Filter (AOTF). After that, a beam with a quasi-monochromatic wavelength is projected on the detectors through a convergent mirror. VNIS can then be used to analyze one single band of data from the lunar surface. Changing the AOTF driving frequency can modulate the wavelengths of the diffractive optics. Ultimately, all band images and spectral data can be obtained. The main parameters of VNIS are shown in Table 1.

VNIS is the first instrument used for in-situ analysis in a lunar exploration mission which carried an AOTF for spectroscopic analysis. Its core component is an AOTF crystal, which is based on acoustic and optical effects (Ling et al. 2004). As the oscillation frequency of the crystal changes, the wavelength of transmitted monochromatic light changes correspondingly. There have been many successful deep space exploration missions that used AOTF imaging spectrometers. For example,

Table 1 Main Parameters of VNIS

Number	Name	Parameter	
		VNIR Channel	SWIR Channel
1	Spectral range (nm)	450∼950	900∼2400
2	Spectral resolution (nm)	2∼7	3∼11.8
3	Sample interval (nm)	5	5
4	Band	100	300
5	Field of View (°)	8.5×8.5	≥3.6
6	Number of pixels	256×256	1
7	MTF	>0.11	—
8	Detection distance (m)	0.7∼1.3	

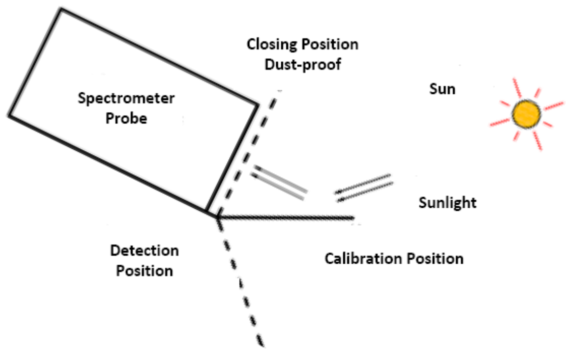

Fig. 4 Based on the position of the calibration target, VNIS works in three operational modes: standby mode (dust proof), detection mode (when the calibration target is fully opened) and calibration mode (when the calibration target is partly opened).

ESA equipped spectrometers on Venus Express and Mars Express satellites based on AOTF technology (Korablev et al. 2002a,b, 2006, 2012; Bertaux et al. 2000, 2007).

One innovative aspect of design for VNIS is the calibration target (He et al. 2011, 2014), the goal of which is to avoid lunar dust coming into the lens when the instrument is not working (see Fig. 4). The other goal is to make VNIS capable of in-situ radiometric calibration. Based on the position of the calibration target, VNIS can be divided into three operating modes: standby mode, detection mode and calibration mode. It is a moving device. When VNIS aims at the lunar surface, it works in detection mode and when VNIS aims at the calibration target, it works in calibration mode.

The three operation modes of VNIS are described as follows:

(1) Standby mode: which means the device is powered on but no data are obtained. In this mode, the calibration target is in the closed position and the lens of VNIS is covered.
(2) Detection mode: which means the instrument works properly and obtains detection data. In this mode, the calibration target is fully opened. The image data and spectral data are obtained as a sequence of bands. In addition, the VIS/NIR and SWIR detectors both collect 20 bands of real-time dark current data. Thus VNIS collects 440 bands of data after one working cycle. The data

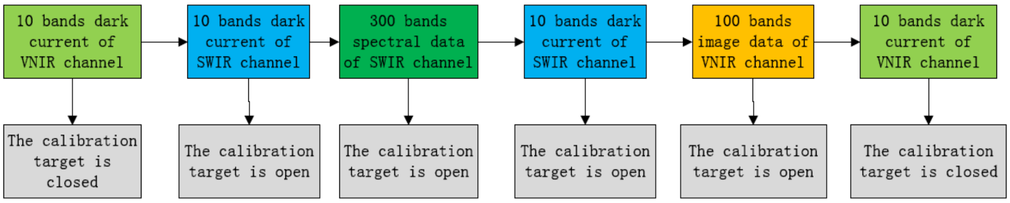

Fig. 5 The data collection sequence used by VNIS.

collection sequence of VNIS is shown in Figure 5. VNIS can also change the center wavelength by changing oscillation frequency of the AOTF cystal to acquire spectral data at a specified wavelength.

(3) Calibration mode: The calibration target is positioned so that it is parallel to the lunar surface, thus the detection target is the calibration target rather than lunar surface. In this mode, the data collection sequence obtained from VNIS is the same as that in detection mode.

3 DATA DESCRIPTION

3.1 Data Acquisition

After the first two lunar days, VNIS made measurements at four different points (E, S3, N203 and N205 in Fig. 6), and obtained data in detection mode four times and calibration mode three times. Data information has been listed in Table 2. The total size of data is 350 MB. All these data have been released to the scientific community.

3.2 Data Preprocessing Pipeline and Products

Like the CE-1 Imaging Interferometer, before the raw data from VNIS are converted to scientific data, a series of data preprocessing steps must be applied, which include channel preprocessing and instrumental preprocessing. Channel preprocessing mainly includes frame synchronization, descrambling and decoding. Instrumental preprocessing mainly includes dark current subtraction, temperature calibration, radiance calibration and geometric calibration. Data used in this paper are Level 2B based on the above calibrations. Different levels of VNIS data have been described in Table 3.

Since the methods for VNIS channel preprocessing are similar to those of other payloads and have been programmed, for example: frame synchronization, descrambling and decoding, we will not describe these methods in detail. As VNIS is the first AOTF type imaging spectrometer to be used for lunar exploration, its instrument preprocessing is shown in Figure 7. The instrument data preprocessing pipeline mainly contains channel data preprocessing and SWIR channel data preprocessing for the two different detectors.

3.3 Data Preprocessing of VNIR Channel

3.3.1 Salt and pepper noise subtraction

Because of differences between the spectral response efficiencies of the CMOS detector's individual pixels, salt and pepper noise is added to the image. This noise is averaged out with a median filter of size 3×3 pixels. In this approach, every image in the spectral image cube (120 bands images, 20 dark images are included) is scanned pixel by pixel. The absolute difference between the center and the surrounding eight pixels' data values is calculated (Fig. 8). The Difference Threshold Value (DTV)

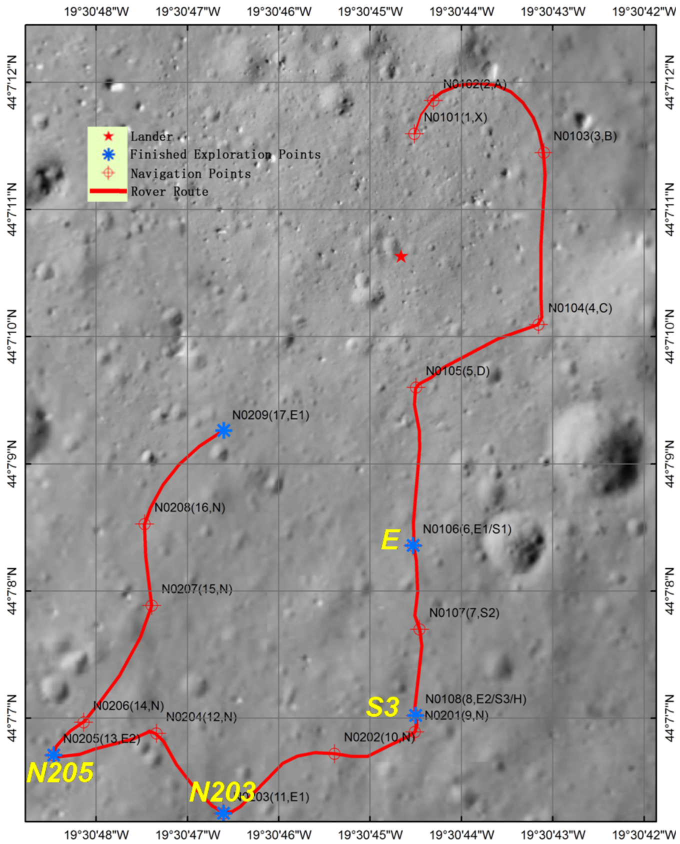

Fig. 6 Map of the path traversed by the Yutu rover and the distribution of detection points.

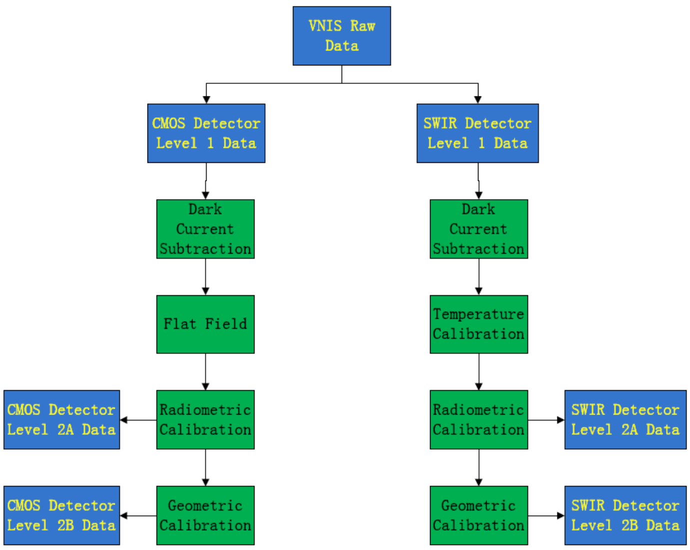

Fig. 7 Preprocessing pipeline and data products for VNIS data.

Table 2 Data Information (Level 2B radiance data)

Number	Detection Point	Working Mode	Detector	Data Level	Data File Name	Data Size
1	E	Detection Mode	CMOS	2B	CE3-BMYK-VNIS-CD-SCI-N-20131223021010-20131223021010-0005-A.2B	25.61MB
			InGaAs	2B	CE3-BMYK-VNIS-SD-SCI-N-20131223021320-20131223021320-0005-A.2B	11kB
		Calibration Mode	CMOS	2B	CE3-BMYK-VNIS-CC-SCI-N-20131223023539-20131223023539-0005-A.2B	25.61MB
			InGaAs	2B	CE3-BMYK-VNIS-SC-SCI-N-20131223023737-20131223023737-0005-A.2B	11kB
2	S3	Detection Mode	CMOS	2B	CE3-BMYK-VNIS-CD-SCI-N-20131224013542-20131224013542-0006-A.2B	25.61MB
			InGaAs	2B	CE3-BMYK-VNIS-SD-SCI-N-20131224013852-20131224013852-0006-A.2B	11kB
3	N203	Detection Mode	CMOS	2B	CE3-BMYK-VNIS-CD-SCI-N-20140112144940-20140112144940-0007-A.2B	25.61MB
			InGaAs	2B	CE3-BMYK-VNIS-SD-SCI-N-20140112145252-20140112145252-0007-A.2B	11kB
		Calibration Mode	CMOS	2B	CE3-BMYK-VNIS-CC-SCI-N-20140112151510-20140112151510-0007-A.2B	25.61MB
			InGaAs	2B	CE3-BMYK-VNIS-SC-SCI-N-20140112151707-20140112151707-0007-A.2B	11kB
4	N205	Detection Mode	CMOS	2B	CE3-BMYK-VNIS-CD-SCI-N-20140114163112-20140114163112-0008-A.2B	25.61MB
			InGaAs	2B	CE3-BMYK-VNIS-SD-SCI-N-20140114163422-20140114163422-0008-A.2B	11kB
		Calibration Mode	CMOS	2B	CE3-BMYK-VNIS-CC-SCI-N-20140114165642-20140114165642-0008-A.2B	25.61MB
			InGaAs	2B	CE3-BMYK-VNIS-SC-SCI-N-20140114165839-20140114165839-0008-A.2B	11kB

is set to 50, and the Point Threshold Value (PTV) is set to 6; if the number of absolute differences which are greater than DTV exceeds the PTV, then the center pixel is considered to be salt and pepper noise, and its value is replaced by the median value of the surrounding eight pixels.

3.3.2 Dark current subtraction

Dark current subtraction has the goal of eliminating the effect of electrical background noise. It is mainly affected by the integration time, gain and temperature. The dark current from the CMOS

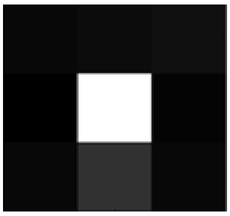

Fig. 8 The salt and pepper noise in the region of size 3×3 pixels.

Table 3 VNIS Data Products and Description

Payload	Data Level	Data Description
	Level 0A	After channel processing, unpacked, and marked in time code with VNIS.
	Level 0B	Based on Level 0A data, but with further ordering, optimal splicing, de-replication, source package header removal, and generate data blocks for VNIS.
VNIS	Level 1	Based on Level 0B data, but with the raw measurements converted to useful physical quantities, framed by detecting cycle (a lander detecting cycle is an earth day, and a rover detecting cycle is a period of time from a scientific exploration mission planning start to end).
	Level 2A	Pepper noise subtraction, dark subtraction, temperature calibration, flat field and radiance conversion using preflight and in-situ calibration coefficient.
	Level 2B	Add the instrument's parameters: focal length, pixel size, and principal point position. Add the rover location and center point location. Add the geometric information include the center point and four corner points' incidence angle, azimuth angle and phase angle.

detector array was calculated through collecting real-time dark current images at different bands and with different integrating times (Xu 2013). The algorithm for dark current subtraction is as follows:

(1) The 20 real-time dark current images are divided into four groups, with each group containing five dark current images from the same band. Then, the mean dark current image from each group is derived;
(2) The four derived mean dark current images are averaged by a median filter with a kernel size of 5 × 5 pixels;
(3) A least squares linear regression method is used to derive the relationship between dark current and integration time for each pixel, and then the slope matrix $k(x, y)$ and intercept matrix $b(x, y)$ are calculated;
(4) The dark current image of each band is calculated by Equation (1), where $DN_{\rm dark}(\lambda, x, y)$ is the dark current of band λ at pixel (x, y) and $\mathrm{Int}T(\lambda)$ is the integration time of band λ.

$$DN_{\rm dark}(\lambda, x, y) = k(x, y) \times \mathrm{Int}T(\lambda) + b(x, y). \tag{1}$$

(5) The dark current is subtracted by Equation (2)

$$DN_{\rm after\_dark}(\lambda, x, y) = DN(\lambda, x, y) - DN_{\rm dark}(\lambda, x, y). \tag{2}$$

3.3.3 Nonuniformity correction

Nonuniformity correction is a necessary step in processing the data from the imaging system for suppressing nonuniformity in images caused by optics, AOTF, etc. It is described by the following equation

$$DN_{\rm uniformity}(\lambda, x, y) = DN_{\rm after\_dark}(\lambda, x, y) \times M_{\rm VNIR}(\lambda, x, y)\,, \tag{3}$$

where $DN_{\rm uniformity}(\lambda, x, y)$ is the data value after nonuniformity correction and $M_{\rm VNIR}(\lambda, x, y)$ is the nonuniformity correction coefficient provided by the manufacturer of the VNIS.

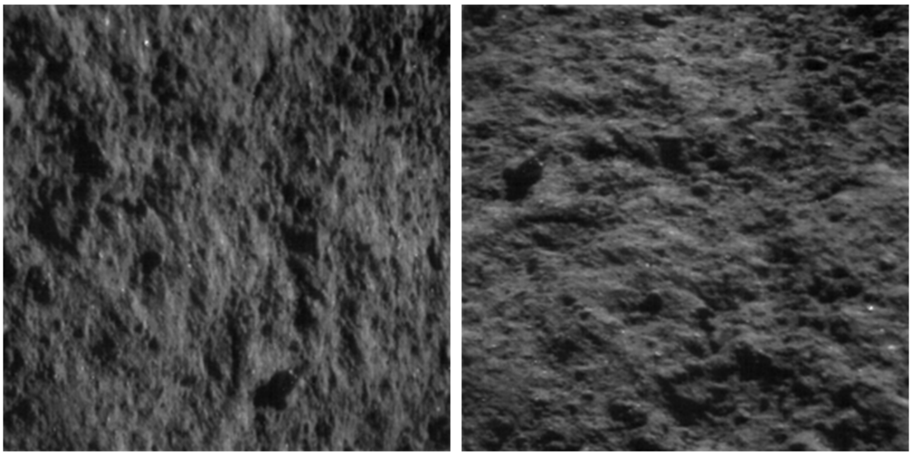

Fig. 9 The radiance images before rotation and transposition (*left*) and after rotation (*right*).

3.3.4 Radiometric calibration

Radiometric calibration is a way to convert the value measured by VNIS to the absolute physical quantity of spectral radiance. It is calculated by the following formula

$$\mathrm{Radiance}_{\mathrm{VNIR}}(\lambda, x, y) = DN_{\mathrm{after\_dark}}(\lambda, x, y) \times N_{\mathrm{VNIR}}(\lambda, x, y), \tag{4}$$

where $\mathrm{Radiance}_{\mathrm{VNIR}}(\lambda, x, y)$ is the spectral radiance data value, $DN_{\mathrm{after\_dark}}(\lambda, x, y)$ is the data value after nonuniformity correction and $N_{\mathrm{VNIR}}(\lambda, x, y)$ is the radiometric calibration coefficient provided by the VNIS manufacturer.

The spectral radiance images must be transposed and rotated after radiometric calibration. This is mainly due to design of the optical system and the readout method used by the CMOS detector. The data readout sequence of CMOS is done column by column, so one line of the scientific image is mapped to one column of the raw image from CMOS. In addition, the image formed at the focal plane of the CMOS detector has a 180° rotation, so the image cube for radiance must be rotated toward the right (Fig. 9).

3.4 Data Preprocessing of the SWIR Channel

3.4.1 Dark current subtraction

The detector adopted by VNIS in the SWIR channel is an InGaAs single element detector, and the readout circuit of this single element detector was designed to have a fixed gain and integration time. So, the dark current could be considered to be electrical noise from the detector itself and the response of unmodulated zero-order stray light signal which is constant at a certain temperature. The method used for dark current subtraction of the SWIR channel is given as follows:

(1) The mean dark current is derived by the following expression

$$DN_{\mathrm{dark}} = \frac{1}{20}\left(\sum_{1}^{10} DN_{\mathrm{dark(front)}}(i) + \sum_{1}^{10} DN_{\mathrm{dark(end)}}(i)\right), \tag{5}$$

where DN_{dark} is the mean dark current, $DN_{\mathrm{dark(front)}}(i)$ is the dark current data value from the first ten bands and $DN_{\mathrm{dark(end)}}(i)$ is the dark current data value from the last ten bands.

(2) The dark current is subtracted with Equation (6)

$$DN_{\mathrm{after\_dark}}(\lambda) = DN(\lambda) - DN_{\mathrm{dark}}(\lambda). \tag{6}$$

3.4.2 Correction for Effect of Temperature

Unlike the VNIR channel, the InGaAs detector adopted in the SWIR channel of VNIS is very sensitive to temperature. The detector's spectral response will change when its temperature changes. Moreover, the beam splitter in VNIS, the AOTF crystal, is driven by a Radio Frequency (RF) power amplifier, and the performance of AOTF is directly affected by the RF. The efficiency of the RF will decline when its temperature goes up, and the light flux received by the InGaAs detector will be affected. After dark current subtraction, correction for the effect of temperature must be done before radiometric calibration. According to the real-time temperature data of the InGaAs detector and the RF, the temperature characteristics of the detector and RF amplifier are first modeled, and then calibration parameters are derived to calibrate data at different temperature environments to the same standard temperature used in a laboratory. The equation describing the correction for the effect of temperature is as follows

$$\mathrm{ratio}_{\mathrm{SWIR}}(\lambda) = \mathrm{ratio}_D(T_D(\lambda)) \cdot \mathrm{ratio}_{\mathrm{RF-fit}}(T_{RF}(\lambda)), \tag{7}$$

$$DN_{\mathrm{correction}}(\lambda) = DN(\lambda) \cdot \mathrm{ratio}_{\mathrm{SWIR}}(\lambda). \tag{8}$$

where $\mathrm{ratio}_D(T_D(\lambda))$ is the detector's temperature correction parameter, $\mathrm{ratio}_{\mathrm{RF-fit}}(T_{\mathrm{RF}}(\lambda))$ is the RF's temperature correction parameter, and $DN(\lambda)$ and $DN_{\mathrm{correction}}(\lambda)$ are data values before and after temperature correction respectively. For more details on correction for the effect of temperature, please refer to Xu (2013).

3.4.3 Radiometric calibration

Since the SWIR channel is not an imaging spectrometer, the radiometric calibration equation is written as follows

$$\mathrm{Radiance}_{\mathrm{SWIR}}(\lambda) = DN_{\mathrm{after\_temperature}}(\lambda) \times M_{\mathrm{SWIR}}(\lambda), \tag{9}$$

where $\mathrm{Radiance}_{\mathrm{SWIR}}(\lambda)$ is the SWIR channel spectral radiance data value, $DN_{\mathrm{after\_temperature}}(\lambda)$ is the data value after correction for the effect of temperature is applied, and $M_{\mathrm{SWIR}}(\lambda)$ is the radiometric calibration coefficient provided by the manufacturer of the VNIS, which has been calibrated by a laboratory radiometric experiment and refined by a lunar in-situ detection using a calibration target (Xu et al. 2014b).

3.5 Evaluation of Accuracy in Radiance Data

VNIS data released are Level 2A and 2B radiance data, and the accuracy of radiance data is important for identification and quantification of minerals from radiance data. The radiance data are evaluated by comparing data from a calibration target after radiometric calibration with its theoretical radiance values after solar irradiation. The relative error is calculated from the following expression

$$\delta = \frac{\sum_{i=1}^{N} \left| \frac{S_{\mathrm{VNIS},i} - S_{SS,i}}{S_{SS,i}} \right|}{N} \times 100\%. \tag{10}$$

In the equation, δ is the relative error, $S_{\mathrm{VNIS},i}$ is the radiance data of a given band, and $S_{SS,i}$ is the theoretical radiance values after solar irradiation. The theoretical radiance data are calculated with the following steps:

(1) The solar irradiance data of Gueymard (2004) are used as incident light;

(2) Given the center wavelengths and spectral resolution data of VNIS, Gaussian models are used to calculate the spectral response of every band for VNIS, then the solar irradiance is resampled by the spectral response curves of VNIS;

(3) The theoretical radiance is calculated with the following expression

$$N_{\lambda\_\mathrm{cali}} = W_{\lambda\_\mathrm{solar}} \times (\alpha_{\mathrm{solar\_elev}}) \times BRF_{\mathrm{cali}}(\alpha_{\mathrm{solar\_elev}}, \beta_{\mathrm{rover\_azim}}) , \tag{11}$$

where $W_{\lambda\_\mathrm{solar}}$ is the solar irradiance after resampling the spectrum, $BRF_{\mathrm{cali}}(\alpha_{\mathrm{solar\_elev}}, \beta_{\mathrm{rover\_azim}})$ is the bidirectional reflectance factor of the calibration target at the solar elevation angle α and the rover's azimuth angle β, and $N_{\lambda\_\mathrm{cali}}$ is the theoretical radiance.

For example, the radiance data in calibration mode for detection point E are used to calculate the relative error. A comparison of the result between radiance after radiometric calibration and its theoretical radiance is shown in Figure 10. We can see that the radiance spectrum after radiometric calibration fits well with the theoretical radiance values. We can also see that radiance in the SWIR channel fits better than the VNIR channel, which indicates the precision of radiometric calibration for the SWIR channel is superior to that of the VNIR channel. The relative errors of the VNIR and SWIR channels are 4.13% and 1.05% respectively, and the relative error in all the bands is only 1.82%, which demonstrates that VNIS has a good precision for radiance calibration.

4 METHODS FOR REFLECTANCE CONVERSION AND MINERAL IDENTIFICATION

4.1 Reflectance Conversion

Reflectance data are basic for identification and quantification of minerals, the precision of which directly affects the precision of the final results. Since the CE-3 lander and Yutu rover landed in the northwest part of Mare Imbrium, the detection area does not include the Cayley Plains area, which is the standard area used for calibrating reflectance data from the Moon acquired by spaceborne imaging (Pieters et al. 2009). However, this method is not suitable for VNIS data. After the ground validation experiment (Liu et al. 2013, 2014), the reflectance analysis method described by Liu et al.

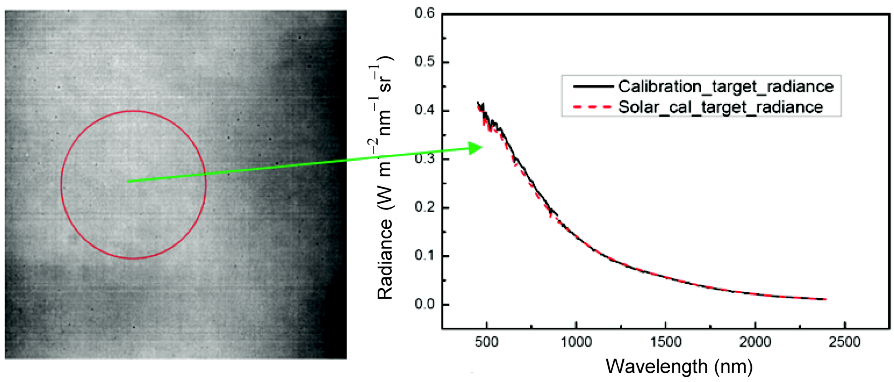

Fig. 10 Radiance data for the calibration target detected at point E (The red circle is the location of the SWIR detector's field of view in the VNIR image, the center point of the circle is located at (96, 128) of the image and the radius is 54 pixels). The black line shows the radiance data after radiometric calibration and the red line indicates values for the theoretical radiance after solar irradiation.

(2013) is adopted and the formula is as follows

$$R_j = \frac{\pi I_j}{F(\lambda)\cos(i)}, \tag{12}$$

where R_j is the band reflectance of VNIS. I_j represents the radiance data after radiometric calibration, $F(\lambda)$ is the solar irradiance (Gueymard 2004) resampled by the VNIS band-pass, and $\cos(i)$ is the cosine of the solar incident angle. The reflectance data of the four detection points are plotted in Figure 11.

As shown in Figure 11, reflectance data from two of the four detection points are found to be discontinuous at the boundary of the two channels. To correct this problem, reflectance data from the SWIR channel are selected as the standard since they are more stable and have smaller spectral jitter, then the translation factor (reflectance ratio between band 900 nm and band 895 nm) is calculated to make VNIR channel reflectance be continuous in the SWIR channel. The two discontinuous reflectance data after gap shifting are shown in Figure 12.

4.2 Identification of Minerals

The main minerals on the lunar surface have obvious absorption features from 450 nm to 2400 nm, such as pyroxene and olivine. The absorption features of pyroxene are evident near 1000 nm and 2000 nm. The absorption features of olivine broaden and deepen near 1000 nm, and it also makes the center wavelength of the absorption change to a longer wavelength (Adams 1974; Burns 1993). Since there are relationships between spectral parameters and main minerals on the Moon, we could identify the main mineral types on the lunar surface by their spectral parameters (Adams 1974; Gaffey et al. 2002; Varatharajan et al. 2014).

We used the modified approach of Varatharajan et al. (2014) to investigate the spectral composition of the CE-3 landing site. In this approach, spectral parameters derived are Band Centers (BCs) and the Integrated Band Depth Ratio (IBDR). A BC1-IBDR plot reveals information about the olivine content in an olivine-pyroxene mixture, and a BC-BC plot shows characteristics of the BCs of orthopyroxenes and clinopyroxenes, which indicate that the monomineralic low-Ca pyroxenes cluster at the bottom of the left corner of the BC-BC plot, and high-Ca pyroxenes cluster at the top right corner. The method is described as follows:

(1) Smoothing the reflectance spectra with a three-point moving average;
(2) Spectral continuum removal by ENVI software (Fig. 13);
(3) Evaluation of the BCs using a second-order polynomial fit around minima in the bands (Fig. 14);
(4) Evaluation of the IBDR using Varatharajan's approach. IBD 1000 and IBD 2000 are given by the following equations:

$$\mathrm{IBD1000} = \sum_{N=0}^{94} R(740 + 10n)/R_{\mathrm{c}}(740 + 10n)\,, \tag{13}$$

$$\mathrm{IBD2000} = \sum_{N=0}^{35} R(1680 + 20n)/R_{\mathrm{c}}(1680 + 20n)\,, \tag{14}$$

$$\mathrm{IBDR} = \frac{\mathrm{IBD2000}}{\mathrm{IBD1000}}\,, \tag{15}$$

where R is a single band reflectance and R_{c} is the reflectance after continuum removal. The beginning and ending wavelengths of the absorption features near 1000 nm are 740 nm and 1680 nm respectively. In addition, the beginning and ending wavelengths of the absorption features near 2000 nm are 1680 nm and 2380 nm respectively.

(5) The scatter plots of BC-BC and BC1-IBDR are used to identify the main minerals on the Moon.

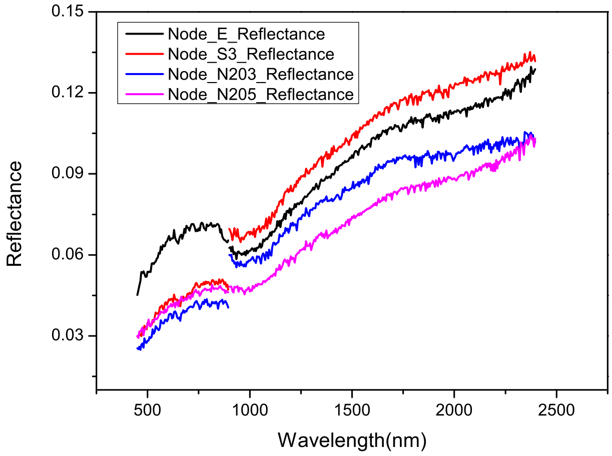

Fig. 11 The reflectance results of the four detection points.

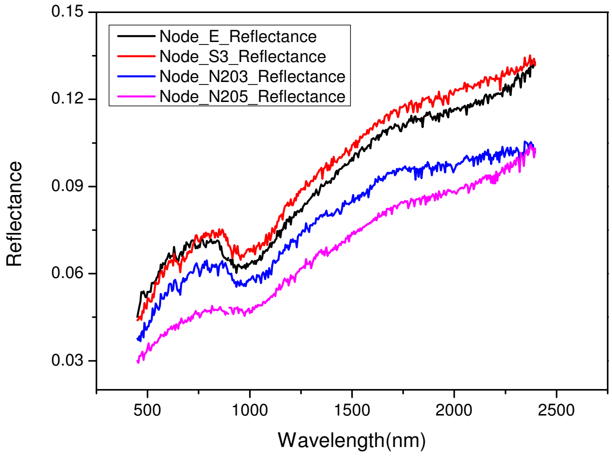

Fig. 12 Reflectance data of the four detection points after the gap shift is applied.

5 PRELIMINARY RESULTS AND DISCUSSION

5.1 Spectral Feature Analysis

From Figure 12, there are obvious absorption features near 1000 nm in data from all four detection points, but the absorption feature of N205 is wider and shallower than the other three data. As revealed by Figure 13, the spectra from detection points S3 and N203 have no or very weak absorption features near 2000 nm.

Reflectance spectral data were also evaluated by comparing VNIS data with M^3 and data from samples of lunar mare. The M^3 reflectance spectrum of the CE-3 landing site was selected (pixel located at (283, 15633), which has file name $M3G20090207T061610\_V01\_RFL.IMG$). Reflectance spectra of nine samples of lunar mare that were returned by the Apollo program were also selected for comparison. The results are shown in Figure 15.

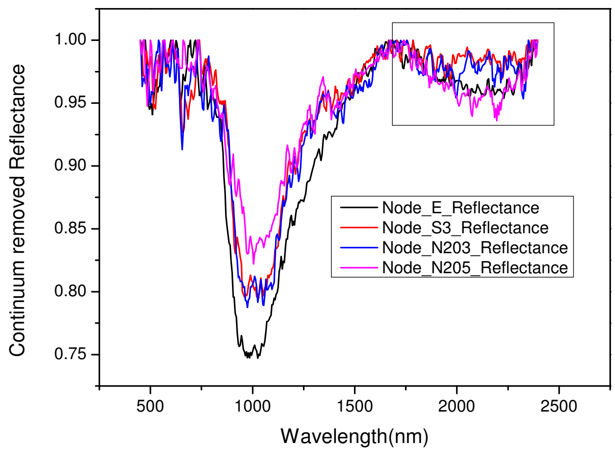

Fig. 13 Reflectance after the continuum was removed from the four detection points.

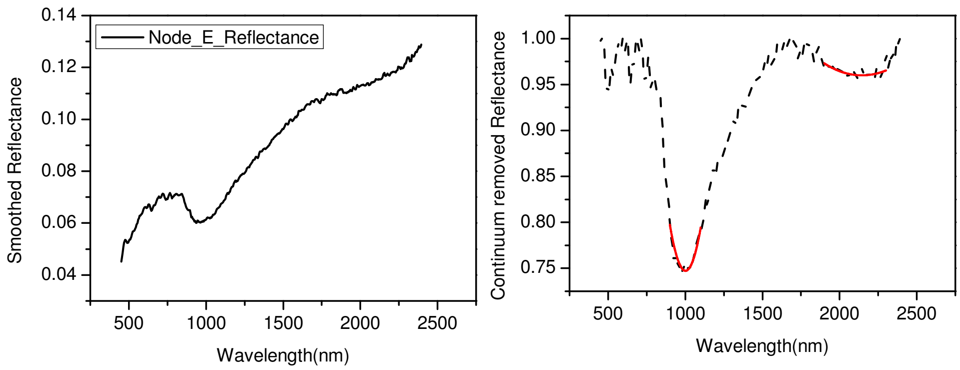

Fig. 14 Computation of the BCs. *Left*: the reflectance spectra of detection point E. *Right*: BC1 and BC2 after smoothing and continuum removal.

We can see that all the reflectance data have similar absorption features near 1000 nm except lunar sample 71061. VNIS reflectance also has a weak absorption feature between 1750∼2400 nm, but the slope of VNIS reflectance data at longer wavelengths is lower than that in the lunar sample.

The difference between VNIS reflectance data taken with M^3 and data taken from samples of lunar mare can probably be described as follows: (1) the spatial coverage between data from VNIS, M^3 and lunar mare samples is not the same; (2) the viewing geometry between VNIS, M^3 and lunar mare sample is different; (3) the conditions of the samples of lunar mare in the laboratory are not the same as on the lunar surface.

5.2 Analysis of Mineralogical Features

Since the spectra detected at points S3 and N203 have no or very weak absorption features near 2000 nm (Fig. 13), we only take the spectra of points E and N205 into account. The result is shown in Figure 16.

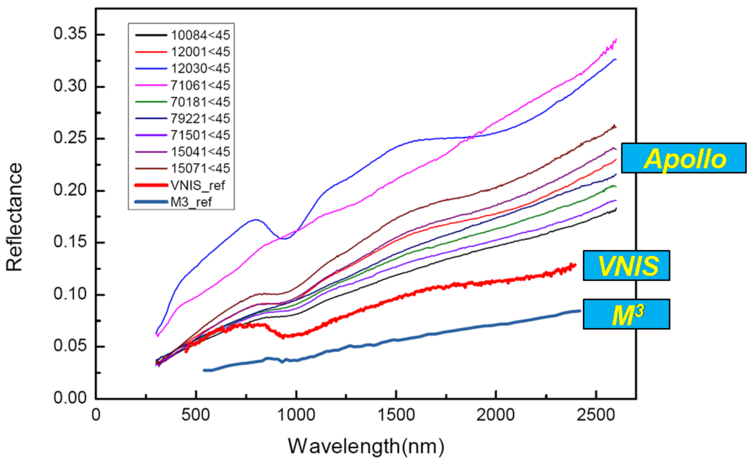

Fig. 15 VNIS spectral features of detection point E compared with samples from M^3 and samples of lunar mare that were returned by the Apollo program.

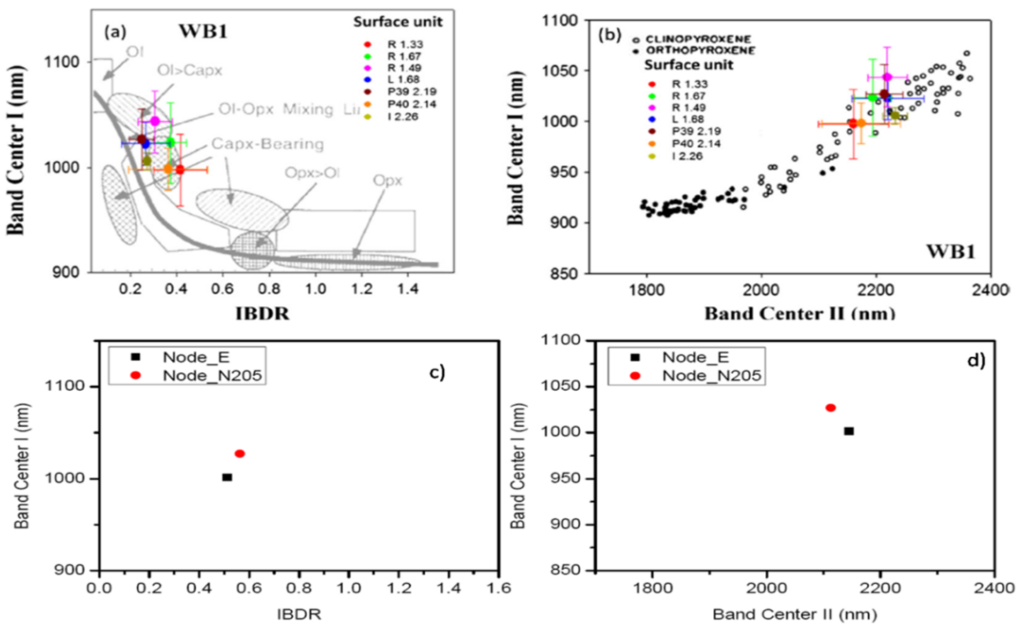

Fig. 16 (a) and (b) are BC1-IBDR and BC-BC plots of lunar western nearside results by Varatharajan et al. (2014) for reference. (c) and (d) are BC1-IBDR and BC-BC plots of data collected from the traverse of the surface by the Yutu rover.

By comparing (a) and (c) in Figure 16, the mineralogy of detection points E and N205 should be a mixture of pyroxene and olivine, and the olivine content at point N205 should be higher than that at point E due to a higher BC1 value. By comparing (b) and (d) in Figure 16, the pyroxene type detected at points E and N205 should be high-Ca pyroxene (or clinopyroxene).

The spectra (Fig. 13) show that the compositions detected at points S3 and N203 are mainly olivine-rich because of the obvious absorption features near 1000 nm and have no or very weak absorption features near 2000 nm.

6 CONCLUSIONS

In this paper, the principle and working mode of VNIS are first introduced. Based on the released Level 2B radiance data, we mainly describe the data preprocessing methods, and the approaches for reflectance analysis and mineral identification. The preliminary spectral and mineralogical features of the landing site are also discussed. After data preprocessing, the relative errors in the VNIR and SWIR channels are 4.13% and 1.05% respectively, which demonstrate VNIS has good precision for radiometric calibration. There are obvious absorption features near 1000 nm in data from all four detection points, but the detection points S3 and N203 have no or very weak absorption features near 2000 nm after removal of the continuum. Mineralogical results reveal that the mineralogy of detection points E and N205 should be a mixture of high-Ca pyroxene and olivine, and the composition of detection points S3 and N203 are mainly olivine-rich. Since there are no obvious absorption features of plagioclase near 1250 nm, we could not identify plagioclase at the CE-3 landing site.

Further work is still needed to improve the quality of VNIS data. Photometric correction must be done before mineral quantification can be performed, and the refinement of data processing is also needed.

Acknowledgements This study was supported by the National Natural Science Foundation of China (Grant Nos. 41274182 and 11273037).

References

Adams, J. B. 1974, J. Geophys. Res., 79, 4829

Bertaux, J.-L., Fonteyn, D., Korablev, O., et al. 2000, Planet. Space Sci., 48, 1303

Bertaux, J.-L., Nevejans, D., Korablev, O., et al. 2007, Planet. Space Sci., 55, 1673

Bugiolacchi, R., & Guest, J. E. 2008, Icarus, 197, 1

Burns, R. G. 1993, Mineralogical Applications of Crystal Field Theory (Cambridge: Cambridge Univ. Press)

Cahill, J. T. S., Lucey, P. G., & Wieczorek, M. A. 2009, Journal of Geophysical Research (Planets), 114, 9001

Elkins Tanton, L. T., Van Orman, J. A., Hager, B. H., & Grove, T. L. 2002, Earth and Planetary Science Letters, 196, 239

Gaffey, M. J., Cloutis, E. A., Kelley, M. S., & Reed, K. L. 2002, in Asteroids III, ed. W. F. B. Jr., A. Cellino, P. Paolicchi, & R. P. Binzel (Tucson: University of Arizona Press), 183

Fu, X. H., Li, C.-L., Zhang, G.-L., et al. 2014, RAA (Research in Astronomy and Astrophysics), 14, 1595

Gueymard, C. A. 2004, Solar Energy, 76, 423

He, Z. P., Shu, R., & Wang, J. Y. 2011, in International Symposium on Photoelectronic Detection and Imaging 2011, International Society for Optics and Photonics, 819625

He, Z.-P., Wang, B.-Y., Lü, G., et al. 2014, RAA (Research in Astronomy and Astrophysics), 14, 1567

Hiesinger, H., Jaumann, R., Neukam, G., & Head, J. W. 2000, J. Geophys. Res., 105, 29239

Ip, W.-H., Yan, J., Li, C.-L., & Ouyang, Z.-Y., 2014, RAA (Research in Astronomy and Astrophysics), 14, 1511

Jolliff, B. L., Gillis, J. J., Haskin, L. A., Korotev, R. L., & Wieczorek, M. A. 2000, J. Geophys. Res., 105, 4197

Korablev, O., Bertaux, J.-L., Grigoriev, A., et al. 2002a, Advances in Space Research, 29, 143

Korablev, O. I., Bertaux, J.-L., Dimarellis, E., et al. 2002b, in Society of Photo-Optical Instrumentation Engineers (SPIE) Conference Series, 4818, Infrared Spaceborne Remote Sensing X, ed. M. Strojnik & B. F. Andresen, 261

Korablev, O., Bertaux, J.-L., Fedorova, A., et al. 2006, Journal of Geophysical Research (Planets), 111, 9

Korablev, O., Fedorova, A., Bertaux, J.-L., et al. 2012, Planet. Space Sci., 65, 38
Ling, B., Dennis, G. I., Miller, H. M., Spaine, T. W., & Carnahan, J. W. 2004, Progress in Quantum Electronics, 28, 67
Liu, B., Liu, J.-Z., Zhang, G.-L., et al. 2013, RAA (Research in Astronomy and Astrophysics), 13, 862
Liu, B., Liu, J., Zhang, G., et al. 2014, Chinese Journal of Geochemistry, 33, 86
Ohtake, M., Matsunaga, T., Yokota, Y., et al. 2010, Space Sci. Rev., 154, 57
Ouyang, Z. Y. 2005, Introduction to lunar science (Beijing: China Astron Publ House)
Pieters, C. M. 1999, in Workshop on New Views of the Moon II: Understanding the Moon Through the Integration of Diverse Datasets, 47
Pieters, C. M., Sunshine, J. M., Fischer, E. M., et al. 1993, J. Geophys. Res., 98, 17127
Pieters, C. M., Boardman, J., Buratti, B., et al. 2009, Current Science, 96, 500
Qiao, L., Xiao, L., Zhao, J., & Huang, Q. 2013, Scientia Sinica Physica, Mechanica & Astronomica, 43, 1370
Schaber, G. G. 1969, Geologic Map of the Sinus Iridum Quadrangle of the Moon (Washington DC: US Geological Survey)
Tompkins, S., & Pieters, C. M. 1999, Meteoritics & Planetary Science, 34, 25
Varatharajan, I., Srivastava, N., & Murty, S. V. S. 2014, Icarus, 236, 56
Williams, D. A., Greeley, R., Neukum, G., Wagner, R., & Kadel, S. D. 1995, J. Geophys. Res., 100, 23291
Xu, R. 2013, PhD Thesis, Calibration of AOTF imaging spectrometer in deep-space exploration application, University of Science and Technology of China
Xu, R., He, Z. P., Chen, K., et al. 2014, Journal of Infrared and Milimeter Waves, 33, 327
Xu, R., He, Z. P., Ma, Y. H., Liu, B., & Wang, J. Y. 2014b, International Journal of Emote Sensing, Submitted
Yamamoto, S., Matsunaga, T., Ogawa, Y., et al. 2011, Geoscience and Remote Sensing, IEEE Transactions on, 49, 4660
Zhao, J., Huang, J., Qiao, L., et al. 2014, Science China Physics, Mechanics, and Astronomy, 57, 569